Structural changes in FeOx/γ-Al2O3 catalysts during ethylbenzene dehydrogenation

MEDIERO-MUNOYERRO, M J, MCGREGOR, J, MCMILLAN, L, AL-YASSIR, N, BINGHAM, Paul <http://orcid.org/0000-0001-6017-0798>, FORDER, Sue, GORIN, Colin, AL-KHATTAF, S, GLADDEN, L F and MIDGLEY, P A

Structural changes in FeO_x/γ-Al_2O_3 catalysts during ethylbenzene dehydrogenation

M. J. Mediero-Munoyerro,[a] J. McGregor,[b§*] L. McMillan,[b] N. Al-Yassir,[c] P.A. Bingham,[d] S.D. Forder,[d] C. Gorin,[d] S. Al- Khattaf,[c] L. F. Gladden[b] and P. A. Midgley[a]

[a]University of Cambridge, Department of Materials Science and Metallurgy, 27 Charles Babbage Road, Cambridge, CB3 0FS UK.
[b]University of Cambridge, Department of Chemical Engineering and Biotechnology, New Museums Site, Pembroke Street, Cambridge CB2 3RA, UK.
[c]Center of Research Excellence in Petroleum Refining and Petrochemicals, King Fahd University of Petroleum & Minerals, Dhahran 31261, Saudi Arabia.
[d]Materials and Engineering Research Institute, Sheffield Hallam University, City Campus, Sheffield S1 1WB, UK.
[§]present address: University of Sheffield, Department of Chemical and Biological Engineering, Mappin Street, Sheffield S1 3JD, UK.

*james.mcgregor@sheffield.ac.uk

Abstract

The structural changes that occur in a FeO_x/γ-Al_2O_3 catalyst during the dehydrogenation of ethylbenzene in a fluidized CREC Riser Simulator have been investigated. Chemical and morphological changes are observed to take place as a result of reaction. Electron microscopy reveals the formation of needle-like alumina structures apparently enclosing iron oxide particles. The formation of such structures at relatively low temperatures is unexpected and has not previously been reported. Additionally, X-ray diffraction and Mössbauer spectroscopy confirmed the reduction of the oxidation state of iron, from Fe_2O_3 (haematite) to Fe_3O_4 (magnetite). Iron carbides, Fe_3C and ε–Fe_2C, were detected by electron microscopy through electron diffraction and lattice fringes analysis. Carbon deposition (coking) on the catalyst surface also occurs. The observed structural changes are likely to be closely correlated with the catalytic properties of the materials, in particular with catalyst deactivation, and thereby provide important avenues for future study of this industrially important reaction.

1. Introduction

In catalytic systems, there are a number of possible causes of catalyst deactivation: coke deposition on the catalyst surface; chemical phase changes that occur during reaction; and physical degradation after a period of operation[1–5]. In some cases the issues are directly related, *e.g.* phase change can be an important factor contributing to the pulverization of the catalytic material[3]. The structural changes that catalysts undergo during reaction can, however, also lead to the formation of catalytically-active phases[4,6,7] . The formation of different oxides and carbides is well known for iron catalysts, particularly in Fischer-Tropsch synthesis[7,8], during which iron-based materials undergo complex phase changes[9], with the identification of the active phase still disputed[10]. Carbide phases formed *in situ* also play a catalytic role in, *e.g.* dehydrogenation and isomerisation over molybdenum oxycarbides [7] and dehydrogenation over PdC_x species[6].

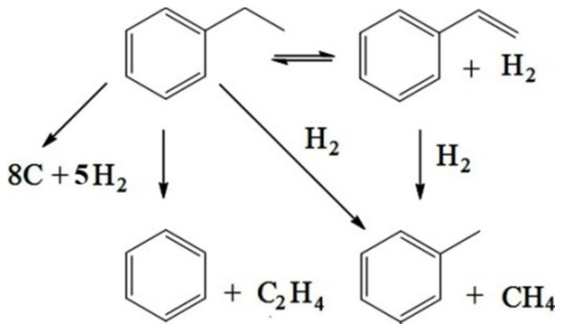

Scheme 1. Reaction scheme for ethylbenzene dehydrogenation[11].

The dehydrogenation of ethylbenzene is a further example of a reaction where Fe based catalysts undergo structural and phase changes as a function of time on stream. Ethylbenzene dehydrogenation is the main route commercially employed in the production of styrene (Scheme 1)[12,13]. This reaction is equilibrium limited and strongly endothermic, and under industrial conditions is normally carried out in fixed bed units operating in adiabatic mode. In the present study, a fluidised bed reactor (CREC Fluidized Riser Simulator) has been used, this reactor operates isothermally. Previous studies have shown that this configuration can overcome the typical diffusional and thermodynamic limitations often present in conventional fixed bed operation[14]. Some of the advantages that the use of fluidized beds presents over traditional fixed beds include: the use of short residence times that minimize cracking thereby

improving the selectivity towards styrene; suitable temperature control of the catalyst; and continuous regeneration[15].

The main causes of catalyst deactivation in ethylbenzene dehydrogenation are coke deposition, reduction of iron oxide, loss and/or redistribution of promoters and physical degradation[3]. Herein, we apply a range of advanced electron microscopy, chemical and spectroscopic techniques to characterise the changes that occur in an unpromoted iron catalyst in a reducing atmosphere under steam-free conditions, thereby accelerating structural changes in the catalyst and facilitating the study of these processes. Understanding the structural changes that occur during reaction is crucial in order to appreciate the dynamic nature of the catalyst during operation in which different structures and phases form, which are not present in the starting material, and which can be directly implicated in both catalytic activity and catalyst deactivation. Only upon understanding the structure of the catalyst under reaction conditions can a full attempt be made at elucidating structure-activity relationships, which are essential in the design of improved catalysts. This work therefore seeks to characterise these changes in an important catalytic system.

2. Experimental

2.1. Catalyst preparation

An iron catalyst supported on γ-Al_2O_3 was prepared using a conventional wet impregnation method. Alumina powder (Condea Chemie GmbH) was slowly added to a solution of iron (III) nitrate hexahydrate in distilled water. The slurry was mixed at room temperature for 2 h and the water was slowly evaporated while stirring. Subsequently, samples were dried at 120 °C overnight followed by calcination in standing air from 25 to 550 °C (1 °C/min ramping rate, 5 h hold time). The final catalyst loading was determined post-synthesis as 21 wt.% Fe.

2.2. Catalytic reaction

The ethylbenzene dehydrogenation reaction was carried out in a fluidized CREC Riser Simulator, developed at the Chemical Reactor Engineering Centre, University of Western Ontario[16]. This bench scale mini-fluidized bed reactor, operated in a batch mode, is able to simulate the conditions of an industrial scale reactor unit, including gas-catalyst contact times and gas velocities. The reactor details and the experimental procedure are described

elsewhere[16–18]. The catalytic reaction was performed isothermally at 500 °C and at atmospheric pressure (before injection) with a contact time of 20 s. Additional screening experiments took place at a range of temperatures (350-550 °C) and contact times (5, 10, 15, 20s), as shown in Table S1. Conversion increases with both temperature and contact time, but little difference in the relative percentages of detected products is observed. For example, at 450 °C the percentage, by mass, of styrene in the product stream varies only between 93.4 % (at a contact time of 20 s) and 96.0 % (at a contact time of 5 s) with smaller variations at other temperatures. Comparing different reaction temperatures at the same contact time it is observed that at a contact time of 5 s the greatest variation in styrene selectivity is between 450 °C, where it comprises 96.5 % of the product stream, and 550 °C, where it comprises 85.2 %. The sample selected for detailed investigation can therefore be considered representative for a broad range of reaction conditions.

The catalyst was fully fluidized at 5000 rpm and the outlet gas flow was monitored by direct injection into a gas chromatograph (Hewlett-Packard 5890A). Three measurements were taken, and the standard deviation in the results was determined to be ±2%. Conversion was calculated from on-line gas-chromatography data as shown in equation 1:

$$\text{Conversion}\,\% = 100 \times \frac{\text{moles of ethylbenzene converted}}{\text{moles of ethylbenzene fed}} \qquad (1)$$

2.3. Characterisation methods

A wide-range of advanced techniques were applied to the characterisation of the fresh and spent catalysts in order to ascertain the changes that the material undergoes during reaction, and which will influence its catalytic performance. All characterisation is conducted *ex situ* and hence the samples are exposed to atmospheric conditions prior to measurement.

2.3.1. Textural properties

The textural properties were characterized by N_2 adsorption measurements at 77 K, using a QuantachromeAutosorb 1-C adsorption analyser. Samples were out-gassed at 220 °C under vacuum (10^{-5} Torr) for 3 h before N_2 physisorption. The BET specific surface area was determined from the N_2 adsorption data in the relative pressure (P/P_0) range 0.06-0.3, and the pore size distribution was calculated using the Barrett-Joyner-Halenda (BJH) method. The

determined textural properties of the FeO_x/γ-Al_2O_3 catalyst employed were: BET surface area of 116 m^2/g; total pore volume of 0.23 cm^3/g; and average pore diameter of 5.80 nm.

2.3.2. X-ray diffraction

Powder X-ray diffraction (XRD) studies were conducted on a Philips X'Pert PW3020 diffractometer (Cu $K\alpha_1$ radiation) at room temperature from 6^o to 85^o 2θ (wide angle). Measurements were performed using a voltage of 40 kV, a current setting 40 mA, a step size of 0.04^o and a time per step of 15 s.

2.3.4. Mössbauer spectroscopy

^{57}Fe Mössbauer spectra were collected at room temperature relative to α-Fe over the velocity range ± 12 mm s^{-1} using a constant acceleration spectrometer with a 25 mCi source of ^{57}Co in Rh. Spectra were fitted using the Recoil analysis software package.

2.3.5. Scanning electron microscopy

Secondary electron micrographs of both fresh and spent FeO_x/γ-Al_2O_3 catalysts were acquired in a scanning electron microscope model Camscan MX2600 FEGSEM operating at 5 keV. Energy dispersive X-ray spectroscopy (EDS) was also employed to differentiate the constituent phases of the specimens. SEM EDS mapping was carried out in a JEOL 5800 LV SEM operating at 15 keV. Samples were mounted on a stub and coated with gold in order to prevent charging.

2.3.6. Transmission electron microscopy

Transmission electron microscopy was conducted on two different microscopes. A Philips CM30 TEM with an accelerating voltage of 250 kV was used to perform electron diffraction experiments on FeO_x/γ-Al_2O_3. Subsequently, a FEI Tecnai F20-G2 FEG TEM operated at 200 kV was used to collect HRTEM images and STEM micrographs using a high angle annular dark field (HAADF) detector. Chemical analysis (EDS) of the samples was carried out in the same instrument.

The specimen preparation for TEM involved grinding powder samples between two clean glass slides. Afterwards, a suspension of the catalyst powder using high purity ether was prepared, allowing a drop of the solution to evaporate on a carbon coated copper grid. The

amount and size of material transferred to the grid was monitored using an optical microscope.

3. Results and discussion

The ethylbenzene dehydrogenation reaction was carried out at 500 °C with a contact time of 20 s over the FeO_x/γ-Al_2O_3 catalyst. Styrene was the main product, comprising 88 % of the detected species by mass, with smaller amounts of benzene (10 %) and toluene (2 %) formed. The remaining gaseous products detected were mainly hydrogen, methane, ethane and ethylene. Ethylbenzene conversion was ~14%.

Powder X-ray diffraction of both the fresh and post reaction catalysts was conducted in order to ascertain any structural changes which occurred as a result of the dehydrogenation reaction. The XRD pattern of the unreacted catalyst indicated that the main phase of the support was γ–Al_2O_3; while the iron was observed to be present as Fe_2O_3. On comparing fresh and post reaction samples (Figure 1), a change in the oxidation state of Fe was detected, which will have been caused by the reducing environment; molecular hydrogen will be present during reaction as a result of dehydrogenation, cracking and thermal decomposition of ethylbenzene[12]. Thus with no steam or any other inert gas present and without any structural promoter to stabilize the Fe^{3+} oxidation state, reduction of the oxide took place, *i.e.* Fe_2O_3 (haematite) was transformed to Fe_3O_4 (magnetite), which is generally accepted as being an inactive phase[19], according to the following reaction:

$$3Fe_2O_3 + H_2 \rightarrow 2Fe_3O_4 + H_2O.$$

Several studies have supported this change in Fe oxidation state[20–24] but some propose that magnetite is, in fact, more selective than haematite[25] and that the catalyst only becomes stable after reduction and a certain time on stream[26]. However, the majority of studies indicate that the reduction of Fe^{3+} containing species should be avoided in order to prevent the deactivation of the catalytic material. This is not only to avoid the formation of inactive phases[27–29], but also because the crystal structure of magnetite (cubic vs. hexagonal hematite) can contribute, along with mechanical forces inside the reactor, to the degradation of the material[3].

In order to gain further insights into the nature of the iron species present, ^{57}Fe Mössbauer spectroscopy of fresh and post-reaction samples was carried out. The acquired spectra were fitted with a single broadened Lorentzian paramagnetic doublet plus 1 sextet (Figure 2a) and 2 broadened Lorentzian paramagnetic doublets plus 2 sextets (Figure 2b). The goodness-of-fit is quantified by reduced χ^2 values of 1.792 for the sample pre-reaction; and 2.288 for the sample post-reaction. The results support XRD analysis by confirming that iron in the fresh catalyst existed predominately as Fe_2O_3, as evidenced by the extracted sextet parameters (Table S2) which are consistent with α-Fe_2O_3[30,31]. Mössbauer spectra also confirm the change in oxidation state in the post-reaction sample through the formation of Fe_3O_4, again as evidenced by the extracted sextet parameters. As discussed earlier, electron diffraction also indicated the presence of small quantities of iron carbides alongside iron oxide phases. Fitting a third sextet representing carbides was attempted, however, its small area (*i.e.* abundance of only a few per cent) made any improvement in fitting by adding this component only statistical and it was therefore not included here. The Mössbauer data are therefore consistent with the presence of a small quantity of iron carbide, but cannot be used to directly to support the electron diffraction analysis.

Electron microscopy studies provide detailed characterisation of the structural properties of catalyst before and after reaction. SEM and EDS yield information on catalyst morphology and the elemental composition of the catalyst (Figure 3); while HAADF STEM (Figures 4-5) and bright field TEM (BFTEM) (Figure 6) allow for a detailed characterisation of the different structural motifs present in the catalyst, in particular the different alumina structures present. These results, and their relationship with catalytic properties of the material, are now discussed.

SEM of the fresh catalyst confirmed a degree of heterogeneity within the catalytic material. As shown in Figure 3, energy dispersive X-ray spectroscopy maps show a segregation of phases. Some regions are Fe-rich whilst others are predominantly alumina. In general, rounded iron oxide particles of 1-2 μm in size, indicated by arrows, appear to be deposited over and between larger alumina grains of size 10-20 μm. In Table 1 the chemical composition (determined using standard ZAF (atomic number, absorption, fluorescence) correction procedures) of different regions of the catalyst, corresponding to those identified as points 1-4 in Figure 3, is summarised.

HAADF STEM and BFTEM images acquired on the fresh catalyst further illustrated the heterogeneity of the microstructures found. A combination of chemical composition from EDS analysis, electron diffraction and the morphology seen in the images is used to definitively identify four kinds of microstructure with different degrees of crystallinity. These are labelled as (i)-(iv) in Figure 4; area (v) is pure Al_2O_3. Microstructures (i)-(iv) had high Fe/Al ratios (*e.g.* area (i) in Figure 4 has an intensity ratio I_{Fe}/I_{Al} of 8.7) together with the presence of oxygen. These data therefore indicate that iron oxide (confirmed to be Fe_2O_3 by X-ray and Mössbauer spectroscopy data) existed in the fresh material with different morphologies defined as:

(i) Highly porous particles of size 500 nm - 2 μm

(ii) Crystalline "rods" of ~500 nm length

(iii) Rounded crystalline particles of size ~ 50-100 nm

(iv) Plate-like structures

As expected, aluminium, iron and oxygen were the strongest signals detected by EDS. However, other elements were detected in small quantities. These were copper (coming from the TEM grids) and, rarely, silicon, which could arise from a detector artefact or an impurity in the support. In addition to areas containing both Fe and Al, some regions were composed of almost pure Al_2O_3, e.g. area (v) indicated on Figure 4. The variation in composition of the different microstructures is quantified in Table 2.

BF images and HAADF micrographs of the post reaction catalyst showed that the microstructures observed in the fresh sample remain after treatment, indicating that the material did not degrade during reaction: some of these microstructures are shown in Figure 5 where the labels refer to the same microstructures as in Figure 4. However, in the post reaction catalyst, needle like structures, not seen in the fresh sample, which appear to contain crystalline particles 20-50 nm in size (indicated by arrows) are observed (Figure 6). These structures emerge directly from the alumina support, with a number appearing in close proximity to each other. HAADF STEM EDS mapping (Figure 7(a)-(c)) indicated that the needles were formed from alumina, while the crystalline particles contained within them were FeO_x: inferred to be Fe_3O_4 on the basis of X-ray and Mössbauer spectroscopy results.

Needle, or whisker, like alumina morphologies have previously been identified in catalytic and related systems. For example MoO_3 has been observed to promote the growth of γ-Al_2O_3 whiskers at temperatures above 850 °C[32]; while the formation of alumina needles has been

observed on FeCrAl foils after oxidation at 950 °C[33]. Such alumina morphologies are typically associated with metastable Al_2O_3 phases, *e.g.* γ- or θ-Al_2O_3[34]. Structural changes have previously been observed to occur in alumina supports under dehydrogenation reaction conditions. For example, a phase change towards a more crystalline form of Al_2O_3 has been observed for VO_x/Al_2O_3 catalysts employed in the dehydrogenation of butane[35]. To the best knowledge of the authors however, such needle like structures have not previously been observed to form in catalytic systems under the temperatures employed herein. That such microstructures form at relatively low reaction temperatures (500 °C) is particularly noteworthy, and may be indicative of a solid-state transformation catalysed by iron species. A further unexpected morphological formation is the apparent enclosure of Fe_3O_4 particles within these needles. While the formation of iron carbides is well-established in many catalytic processes, the co-location of these with the Al_2O_3 needles formed at low temperature is particularly noteworthy.

In addition to needle-like morphologies, BF TEM images also revealed the presence of crystalline dispersed particles of approximately 100 nm size. Analysis of electron diffraction patterns showed the particles to be ε-Fe_2C. In Figure 8(a), a TEM micrograph of one of these particles is shown as an inset together with a corresponding indexed diffraction pattern. Other carbides were also found adjacent to the elongated alumina microstructures described (see Figure 8(b)). Analysis of the lattice fringes indicated that these carbides were Fe_3C (Figure 8(c)). The presence of carbides, as indicated by TEM, is consistent with the results of Mössbauer spectroscopy. These species, although detected in low concentration, could influence catalytic performance: further work needs to be undertaken in order to clarify their role, be it in promoting or deactivating the reaction, or as an inert spectator. Iron carbides have previously been reported in similar systems such as Fischer-Tropsch synthesis[36], where they have been proposed to act as the catalytically active phase[4,7,10]. The mechanism of formation of carbides has been proposed by Ding *et al.* to involve reduction of haematite to magnetite in the surface and bulk regions of the catalyst under a CO atmosphere, and the subsequent transformation of the magnetite surface into iron carbides[8]. Elsewhere, the formation of CO in the direct dehydrogenation of ethylbenzene over CrO_x/Al_2O_3 has been demonstrated and its role in catalyst performance discussed[12]. In the system studied herein, the absence of steam may result in a greater extent of catalyst reduction as compared to reaction systems where steam is present. Additionally, the formation of carbides is a relatively rapid process under these conditions; the contact time in the riser simulator being

20 s. Some carbon is also present on the post-reaction catalyst in the form of carbonaceous deposits, as confirmed by temperature programmed oxidation measurements (Figure S1). Carbon deposition is a well-established feature of dehydrogenation reactions, in particular when the feed consists only of the pure reactant. For iron-based catalysts the formation of such deposits has previously been explained through an iron-carbide cycle mechanism promoted by the reduction of the iron species[37]; the presence of iron carbides allows a similar mechanism to occur in the present study, potentially contributing in part to the formation of the observed deposits.

The comparison of the catalyst after reaction to the fresh material therefore indicates that significant changes are effected as a result of the dehydrogenation reaction. Carbon laydown, or coke, is typical in such reactions; however strcutural changes such as the reduction of iron oxide and formation of iron carbides are likely to play an important role in dictating catalytic performance; while the observation of needle-like alumina structures, formed at relatively low temperatures, encasing Fe_3O_4 particles is particularly notable.

Summary and Conclusions

The dehydrogenation of ethylbenzene over $FeO_x/\gamma\text{-}Al_2O_3$ was carried out in a fluidized CREC Riser Simulator at 500 °C and with a contact time of 20 s in the absence of steam. In order to understand the structural changes that occurred during reaction, a range of techniques were applied, namely: X-ray diffraction, Mössbauer spectroscopy and electron microscopy. The analysis of the data provided by these methods confirmed the reduction of iron from Fe^{3+} to Fe^{2+}, and the presence of carbides after a very short residence time. Of specific note is the formation during reaction of elongated alumina structures containing iron oxide particles emerging from the alumina support. These species and microstructure may play a role in catalyst performance and deactivation, and hence further investigation of these will facilitate the development of structure-activity relationships.

Acknowledgements

The authors express their appreciation to the support from the Ministry of Higher Education, Saudi Arabia, in establishment of the Center of Research Excellence in Petroleum Refining & Petrochemicals at King Fahd University of Petroleum & Minerals (KFUPM). The research leading to these results has received funding from the European Research Council under the

European Union's Seventh Framework Program (No. FP7/2007-2013)/ERC Grant Agreement No. 291522-3DIMAGE.

Electronic Supplementary Information (ESI) available: Catalytic data EB dehydrogenation reaction (Table S1), fitted ^{57}Fe Mössbauer parameters (Table S2) and post-reaction temperature programmed oxidation data (Figure S1).

References

1 C. H. Bartholomew, *Appl. Catal. A Gen.*, 2001, **212**, 17–60.

2 R. Hughes, *Deactivation of catalysts*, Academic Press, 1984.

3 G. R. Meima and P. G. Menon, *Appl. Catal. A Gen.*, 2001, **212**, 239–245.

4 N. Sirimanothan, H. H. Hamdeh, Y. Zhang and B. H. Davis, *Catal. Letters*, 2002, **82**, 181–191.

5 M. Baghalha and O. Ebrahimpour, *Appl. Catal. A Gen.*, 2007, **326**, 143–151.

6 J. McGregor, Z. Huang, E. P. J. Parrott, J. A. Zeitler, K. L. Nguyen, J. M. Rawson, A. Carley, T. W. Hansen, J.-P. Tessonnier, D. S. Su, D. Teschner, E. M. Vass, A. Knop-Gericke, R. Schlögl and Lynn F. Gladden, *J. Catal.*, 2010, **269**, 329–339.

7 C. H. Collett and J. McGregor, *Catal. Sci. Technol.*, 2016, **6**, 367-378.

8 M. Ding, Y. Yang, B. Wu, T. Wang, L. Ma, H. Xiang and Y. Li, *J. Mol. Catal. A Chem.*, 2011, **351**, 165–173.

9 K. Sudsakorn, J. G. Goodwin and A. A. Adeyiga, *J. Catal.*, 2003, **213**, 204–210.

10 E. de Smit, F. Cinquini, A. M. Beale, O. V Safonova, W. van Beek, P. Sautet and B. M. Weckhuysen, *J. Am. Chem. Soc.*, 2010, **132**, 14928–41.

11 G. P. Chiusoli and P. M. Maitlis, *Metal-Catalysis in Industrial Organic Processes*, Royal Society of Chemistry; 1 edition, 2006.

12 S. Gomez Sanz, L. McMillan, J. McGregor, J. A. Zeitler, N. Al-Yassir, S. Al-Khattaf and L. F. Gladden, *Catal. Sci. Technol.*, 2015, **5**, 3782–3797.

13 S. Gomez Sanz, L. McMillan, J. McGregor, J. A. Zeitler, N. Al-Yassir, S. Al-Khattaf and L. F. Gladden, *Catal. Sci. Technol.*, 2016, **6**, 1120–1133.

14 B. K. Abdalla and S. S. E. H. Elnashaie, *J. Memb. Sci.*, 1995, **101**, 31–42.

15 M. M. Hossain, L. Atanda, N. Al-Yassir and S. Al-Khattaf, *Chem. Eng. J.*, 2012, **207-208**, 308–321.

16 D. Lasa, US Patent 5, 102, 1992, 628.

17 M. M. Hossain and H. I. de Lasa, *AIChE J.*, 2007, **53**, 1817–1829.

18 M. M. Hossain and H. I. de Lasa, *Chem. Eng. Sci.*, 2010, **65**, 98–106.

19 C. Kuhrs, Y. Arita, W. Weiss, W. Ranke and R. Schlögl, *Top. Catal.*, 2001, **14**, 111–123.

20 X. Yang, S. Weng, K. Jiang, L. Mao, Y. Euang and K. Jing, *Hyperfine Interact.*, 1992, **69**, 863–866.

21 B. Herzog and H. Rase, *Ind. Eng. Chem. Prod. Res. Dev.*, 1984, **23**, 187–196.

22 M. Muhler, R. Schlögl, A. Reller and G. Ertl, *Catal. Letters*, 1989, **2**, 201–210.

23 M. Muhler, J. Schutze, M. Wesemann, T. Rayment, A. Dent, R. Schlögl and G. Ertl, *J. Catal.*, 1990, **126**, 339–360.

24 W. Huang, W. Ranke and R. Schlögl, *J. Phys. Chem. B*, 2005, **109**, 9202–4.

25 E. H. Lee, *Catal. Rev.*, 1974, **8**, 285–305.

26 P. Courty and J. F. Le Page, *Stud. Surf. Sci. Catal.*, 1979, **3**, 293–305.

27 F. Cavani and F. Trifirò, *Appl. Catal. A Gen.*, 1995, **133**, 219–239.

28 W.J. Pöpel, W. Büchele, A.Deimling, and H. Petersen, DE 4324905 A1, 1995.

29 G.E. Lewis, R. Allen and F.A. Sherrod, US Patent 4804799, 1989.

30 R. E. Vandenberghe, C. A. Barrero, G. M. da Costa, E. Van San and E. De Grave, *Hyperfine Interact.*, 2000, **126**, 247–259.

31 S. J. Oh, D. C. Cook and H. E. Townsend, *Hyperfine Interact.*, 1998, **112**, 59–66.

32 Y.-F. Li, C.-D. Qin and D. H. L. Ng, *J. Mater. Res.*, 2011, **14**, 2997–3000.

33 L. Jia, M. Shen and J. Wang, *Surf. Coatings Technol.*, 2007, **201**, 7159–7165.

34 V. K. Tolpygo and D. R. Clarke, *Mater. High Temp.*, 2000, **17**, 59–70.

35 J. McGregor, Z. Huang, G. Shiko, L. F. Gladden, R. S. Stein, M. J. Duer, Z. Wu, P. C. Stair, S. Rugmini and S. D. Jackson, *Catal. Today*, 2009, **142**, 143–151.

36 G. B. Raupp and W. N. Delgass, *J. Catal.*, 1979, **58**, 361–369.

37 R. . Buyanov, V. . Chesnokov, A. . Afanas'ev and V. S. Babenko, *Kinet. Catal.*, 1977, **18**, 839.

38 P. J. Sheridan, *J. Electron Microsc. Tech.*, 1989, **11**, 41–61.

Table 1. Percentage elemental composition of the fresh $FeO_x/\gamma - Al_2O_3$ catalyst, determined by SEM EDS mapping and point spectra analysis. 1, 2, 3 and 4 correspond to the points indicated in Figure 3.

Element	1	2	3	4
O K	52	58	48	43
Al K	35	23	41	11
Fe K	13	19	11	46

Table 2. HAADF STEM EDS analysis of microstructures found in the fresh material. Areas and points correspond to those shown in Figure 4: values for point (iii) are quoted for one of the two points identified as this microstructure. Intensity (I) values correspond to number of counts in the acquired EDS spectra; quantitative concentration (C) ratios have been determined using standard ZAF correction procedures. K factors are calculated at 200 kV from[38].

	I_{Fe}	I_{Al}	I_{Si}	I_{Fe}/I_{Al}	C_{Fe}/C_{Al}	I_{Fe}/I_{Si}	C_{Fe}/C_{Si}
Area (i)	148.	17.0	-	8.7	9.4	-	-
Point (ii)	70.0	25.0	-	2.8	3.0	-	-
Point (iii)	42.0	6.0	-	7.0	7.6	-	-
Point (iv)	29.0	-	11.0	-	-	2.6	3.6
Area (v)	9.0	240.0	-	0.0	0.0	-	-

Figure Captions

Figure 1. X-ray diffraction patterns of fresh and spent catalysts.

Figure 2. Fitted ^{57}Fe Mössbauer spectra: (a) fresh catalyst, and (b) catalyst post-reaction. Dots show experimental data, pink curve show fitted Mössbauer features and the blue line shows the aggregate fit. Fitted parameters are shown in Table S2.

Figure 3. Low magnification (3500×) SEM (a) and EDS map (b) of the fresh $FeO_x/\gamma–Al_2O_3$ catalyst showing the distribution of iron (red), oxygen (blue) and aluminium (green) elements. Points highlighted in the secondary electron images correspond to EDS point spectra shown in Table 1. Arrows indicate iron oxide particles.

Figure 4. HAADF STEM micrographs of fresh catalyst showing the different microstructures found: Areas (i)-(iv) contain both Fe and Al and are defined as (i) Highly porous particles of size 500 nm - 2 μm; (ii) Crystalline "rods" of ~500 nm length; (iii) Rounded crystalline particles of size ~ 50 - 100 nm; (iv) Plate-like structures; while Area (v) consists of pure Al_2O_3. Analysis of areas (i)-(v) is presented in Table 2.

Figure 5. Low magnification HAADF STEM micrograph of post reaction sample: (i) Highly porous particles of size 500 nm - 2 μm; (iii) Rounded crystalline particles of size ~ 50-100 nm; (v) pure Al_2O_3.

Figure 6. BF TEM micrograph of a nanostructure emerging from the alumina support. Arrows point toward Fe_3O_4 particles.

Figure 7. a) HAADF STEM image of one of the needle like structures found in the post-reaction catalyst; (b) EDS mapping of Area 1 indicated in (a); (c) EDS spectra from Areas 2 and 3 indicated in (a).

Figure 8. (a) Diffraction pattern recorded parallel to the $[1\ \bar{1}\ 0]$ zone axis corresponding to the ε-Fe_2C isolated particle shown in the inset; (b) BF TEM micrograph of an elongated alumina structure containing crystalline particles; (c) HR image of the highlighted area in (b): the strong fringes correspond to the $(2\ \bar{1}\ 0)$ plane.